

Journal of Materials Chemistry A

Accepted Manuscript



This is an *Accepted Manuscript*, which has been through the Royal Society of Chemistry peer review process and has been accepted for publication.

Accepted Manuscripts are published online shortly after acceptance, before technical editing, formatting and proof reading. Using this free service, authors can make their results available to the community, in citable form, before we publish the edited article. We will replace this *Accepted Manuscript* with the edited and formatted *Advance Article* as soon as it is available.

You can find more information about *Accepted Manuscripts* in the [Information for Authors](#).

Please note that technical editing may introduce minor changes to the text and/or graphics, which may alter content. The journal's standard [Terms & Conditions](#) and the [Ethical guidelines](#) still apply. In no event shall the Royal Society of Chemistry be held responsible for any errors or omissions in this *Accepted Manuscript* or any consequences arising from the use of any information it contains.

Visualizing the roles of graphene for excellent lithium storage

Xu-Yi Shan, Guangmin Zhou, Li-Chang Yin, Wan-Jing Yu, Feng Li*, Hui-Ming Cheng*

Received (in XXX, XXX) Xth XXXXXXXXXX 20XX, Accepted Xth XXXXXXXXXX 20XX

DOI: 10.1039/b000000x

5

Graphene has been extensively used in hybrid electrodes for its notable improvement in lithium storage properties. However, direct visualization of the roles of graphene and the origin for the enhancement at nanoscale are highly inadequate, which are difficult to be obtained by *ex-situ* methods. Here, we use *in-situ* transmission electron microscopy to visualize the roles of graphene during lithiation using NiO-graphene hybrid as a model material. We witness that graphene has three roles in a strong-coupled NiO-graphene hybrid: (1) it increases the Li^+ diffusion rate by two orders of magnitude; (2) it strongly improves Li^+ reaction kinetics with NiO at high current densities, and facilitates the homogeneous lithiation of NiO; (3) it severely restricts the expansion of NiO near the interface, ensuring stable electrical contact between graphene and NiO during extended cycling. Combined with the electrochemical measurements and first-principles calculations, this study further verifies the interface-induced graphene enhancement and distinctly provides valuable insights for excellent lithium storage by constructing interfacial binding between graphene and active materials to make full use of the graphene.

With the advent of portable electronics, electric vehicles and large-scale grid energy storage, there is an urgent need for a substantial improvement of lithium ion batteries (LIBs) with both high energy and high power density^{1,2}. However, using conventional LIBs with an insertion mechanism it is difficult to deliver sufficient energy to meet the increasing demands in the long term. A breakthrough in high energy LIBs will lie in the exploration of new materials³. Metal oxides, tin, silicon, *et. al.*, as promising anode electrodes, have attracted significant attention due to their much higher specific capacities than commercial graphite⁴⁻⁹. However, their intrinsically poor lithium ion kinetics and large volume change during cycling severely limits their practical application¹⁰. To overcome these problems, carbon-based hybrids have been extensively studied¹¹⁻¹³. Among the carbonaceous materials, graphene attracts great attention for its high surface area and excellent electronic conductivity¹⁴. Improved lithium storage capacity, coulombic efficiency, cycling and rate capability have been reported for various graphene-based hybrids due to a so-called “synergistic effect”^{15,16}. In our previous study, the synergistic effect was ascribed to the forming of the oxygen bridges between graphene with oxygen functional groups and active material (NiO) by experimental and theoretical evidence¹⁶. However, a direct visualization of the roles of graphene and the origin for the enhancement at nanoscale are highly inadequate.

In-situ techniques, such as scanning electron microscopy¹⁷, atomic force microscopy¹⁸, solid-state nuclear magnetic resonance¹⁹, and synchrotron radiation X-ray tomographic microscopy^{20,21} have been used to explore lithium storage. However, the low spatial resolution of these techniques limits their applications at nanoscale characterization. *In-situ* transmission electron microscopy (TEM) has recently been introduced by Huang *et. al.*²² and exhibited intrinsic advantages to track detailed kinetics at the nanoscale²³. Recently, there have been several *in-situ* TEM reports on the lithiation-delithiation of graphene composites, such as CeO₂, Fe₂O₃ and CoS₂²⁴⁻²⁶. However, in these systems, graphene always used as a support matrix, the specific roles of graphene in the electrochemical process is seldom concerned.

Here we have designed *in-situ* nano-cells inside a TEM chamber to investigate the roles of graphene in lithium storage by using three designed model materials: NiO@graphene, which was synthesized by a hydrothermal reaction; NiO/graphene, which was produced by the simple mechanical mixing of NiO nano-sheets (NSs) and graphene; and NiO NSs (pure NiO NSs only)¹⁶. In contrast to the weak van de Waals force between NiO and graphene in NiO/graphene, a strong interfacial bond between the two components was formed during hydrothermal reaction in NiO@graphene. To construct the *in-situ* nano-cells, these three samples were adhered to Au tips and used as working electrodes. Lithium metal attached to a scanning tunneling microscope (STM) tip served as a counter and reference electrode and its native surface Li₂O layer acted as a solid electrolyte²⁷ (Fig. S1). After applying a -2V bias (relative to lithium), an electrochemical reaction occurred through the following conversion mechanism ($NiO + 2Li^+ + 2e^- = Ni + Li_2O$)⁴.

Experimental section

Materials and methods

Materials: The samples' preparation (NiO@graphene, NiO/graphene and NiO NSs) and the corresponding electrochemical half-battery measurements were described in a previous paper¹⁶. The graphene used here was obtained by chemical exfoliation and thermal reduction of the natural flake graphite powder (NFG). The number of graphene layers used in our experiments is 4-10²⁸.

In-situ TEM setup: The *in-situ* TEM electrochemical measurements were conducted using a TEM-Scanning Tunneling Microscopy sample stage (Nanofactory Instruments AB ST1000) (Fig. S1) inside a FEI Tecnai F20. The HRTEM, STEM and EDPs images were performed using a FEI Tecnai F20 and the EELS mapping were conducted on an FEI Tecnai F30. To minimize the influence of beam irradiation, we used short time beam exposure for imaging and low beam intensity during reaction.

Li^+ diffusion coefficient determined by the EIS method: EIS spectra were collected at open circuit potential for the three samples¹⁶. The inclined lines in the low frequency range are attributed to Warburg impedance, which is associated with Li^+ diffusion in the electrode material. The Li^+ diffusion coefficient was calculated using the following equation:

$$D = (R^2 T^2) / (2 A^2 n^4 F^4 C^2 \sigma^2) \quad (1)$$

Where R is the gas constant; T is the absolute temperature; A is the surface area of the electrode; n is the number of electrons per molecule transferring during the reaction; F is the Faraday constant; C is the concentration of Li^+ and σ is the Warburg coefficient.

The Warburg coefficient σ was obtained using the following equation:

$$Z_{re} = R_e + R_{ct} + \sigma(2\pi f)^{-1/2} \quad (2)$$

Where R_e is the resistance of the electrolyte; R_{ct} is the charge transfer resistance and f is the frequency in the low frequency region. We can conclude that:

$$Z_{re} \propto \sigma f^{-1/2} \quad (3)$$

From equation (3), the plot of Z_{re} vs. the reciprocal root square of the lower frequencies ($f^{-1/2}$) is proportional to σ . Meanwhile, from equation (1), the Li^+ diffusion coefficient D is proportional to σ^{-2} . Hence, we can obtain the values of D for the three samples by an approximate calculation.

First-principles calculations: All calculations in this work were performed using DFT implemented in the Vienna Ab initio Simulation Package (VASP)²⁹, using the generalized gradient approximation (GGA) of Perdew–Burke–Ernzerhof (PBE)³⁰. The electron-ion interactions were described by the projector augmented wave approach (PAW)^{31,32}. The energy cutoff for the plane wave expansion was set to 400 eV. All the geometries were fully relaxed until the forces acting on the atoms were less than 0.01 eV/Å by using only the point for the Brillouin zone sampling. During the relaxations, all atomic positions were relaxed to an energy convergence of 10^{-4} eV (equivalent to a force convergence of 10^{-2} eV/Å). The detailed calculation method was shown in supplementary information.

Results and discussion

Increase of the Li^+ diffusion rate. Because Li^+ diffuses 5~7 orders of magnitude faster in a liquid electrolyte than in a solid electrode material in a battery³³⁻³⁵, it is essential to investigate the solid phase Li^+ diffusion, which plays the key role in achieving a high power density. The process for solid phase Li^+ diffusion in electrode materials with graphene addition consists of two steps in *in-situ* TEM: (1) Li^+ diffusion on the graphene surface; (2) Li^+ diffusion via the interface from graphene to NiO. From the statistical data obtained, the average solid phase Li^+ diffusion rates in the lithiation process were calculated to be 137, 23, and 4 nm/s for NiO@graphene, NiO/graphene and NiO NSs, respectively (Fig. 1a). The Li^+ mobility in NiO@graphene is two orders of magnitude higher than that in NiO NSs and one order of magnitude higher than that in NiO/graphene. The result clearly indicates that graphene can serve as a highway for Li^+ diffusion (See Fig. S2 and Supplementary Movie S1 for the details).

We further evaluated the solid phase Li^+ diffusion in the three samples by electrochemical impedance spectroscopy (EIS). The relationships between Z_{re} (impedance) and $f^{-1/2}$ (frequency) in the low frequency region are shown in Fig. S3, and we estimated that the ratios of the Li^+ diffusion coefficients $D_1(NiO@graphene)/D_2(NiO/graphene)$ and $D_1(NiO@graphene)/D_3(NiO NSs)$ are $1: 4 \times 10^{-1}$ and 5×10^{-2} . The detailed calculation method is shown in Experimental section. The results by *in-situ* TEM measurements have a similar tendency to that calculated from the EIS spectra in electrochemical tests and show a reliable description of the situation in a real battery.

For NiO@graphene and NiO/graphene, the first step for the Li^+ diffusion is the same, so interfacial Li^+ diffusion is responsible for the big difference. To explore the possible mechanism for this distinctly different interfacial Li^+ diffusion, we used electron energy loss spectroscopy (EELS) and scanning transmission electron microscopy (STEM) characterization on the graphene surface. It was found that oxygen-containing functional groups are uniformly distributed on the graphene surface for both samples (Fig. S4, 5), which is well in accordance with the former characterization and the presence of these oxygen-containing functional groups promotes the formation of “oxygen bridges” through a hydrothermal reaction in NiO@graphene¹⁶. To verify this, we investigated the interfacial binding strength between NiO and graphene in the two samples (Fig. S6). In NiO/graphene, the NiO NS can be easily removed from the graphene surface with little damage to the graphene under an external force (Fig. S6b). However, in NiO@graphene, the interfacial interaction is strong enough that both NiO and graphene simultaneously break under an external force (Fig. S6d). The strong interfacial interaction in NiO@graphene ensures the existence of abundant interfacial Li^+ diffusion paths. Once Li^+ reaches the interface through the graphene, it easily transfers from graphene to NiO. In contrast, a simple mechanical mixing in NiO/graphene only can produce a weak interfacial interaction, which will hinder the interfacial Li^+ diffusion.

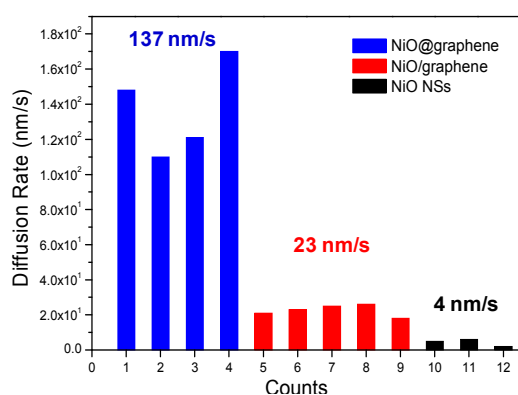


Fig. 1 Li^+ diffusion rates in NiO@graphene (blue), NiO/graphene (red), NiO NSs (black). The average Li^+ diffusion rates measured by *in-situ* TEM are 137, 23, 4 nm/s, respectively.

To further understand the Li^+ diffusion kinetics, first-principles calculations were performed (see Fig. 2). We mainly focused on Li^+ diffusion in three different situations: (1) a graphene surface (Fig. 2a), (2) bulk Li_2O (Fig. 2b,c,e), and (3) a NiO surface (Fig. 2d). The diffusion barrier (E_b) for a Li adatom on the graphene surface was calculated to be 0.29 eV, which is consistent with the previously reported theoretical result (0.28 eV)³⁶. Such a low diffusion barrier implied that graphene could serve as an ultrafast Li^+ diffusion path. For Li^+ diffusion in bulk amorphous Li_2O , the calculated E_b varies from 0.24 to 1.55 eV for eight possible diffusion paths starting from a center Li site, as listed in Fig. 2e. As for Li^+ diffusion on the NiO (111) surface, a large E_b of 2.67 eV was calculated, implying the most difficult Li^+ movement. For NiO NSs, without graphene, the Li^+ only can diffuse via the forming Li_2O after lithiation to move forward, showing a slowest Li^+ diffusion kinetics among the three kinds of samples.

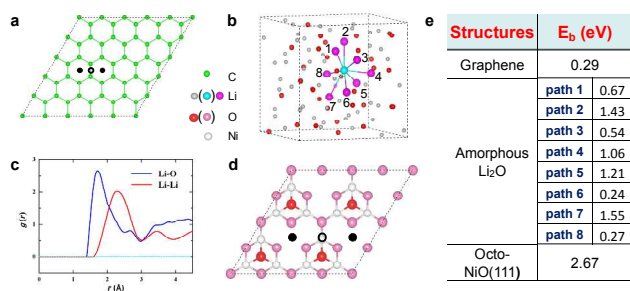


Fig. 2 Schematic of Li^+ diffusion. Li^+ diffusion within (a) graphene, (b) bulk amorphous Li_2O and (d) on a NiO (111) surface with a $p(2 \times 2)$ octopolar reconstruction. (c) The calculated radial distribution function (RDF) $g(r)$ for amorphous Li_2O . The most energetically favorable sites and the transition states for a Li adatom on (a) graphene and (d) a NiO (111) surface with a $p(2 \times 2)$ octopolar reconstruction are represented by solid black ball and open black circles, respectively. The central Li site and its eight neighboring Li sites in amorphous Li_2O (b) are highlighted in light blue and purple, respectively. (e) The calculated energy barriers (eV) for Li^+ diffusion on a graphene surface, within amorphous Li_2O bulk, and on a NiO (111) surface with a $p(2 \times 2)$ octopolar reconstruction.

Improvement of the Li^+ reaction kinetics with NiO. The Li^+ reaction kinetics with NiO is directly related to the power density of a battery^{15,37}. To investigate the difference between the Li^+ reaction kinetics with NiO@graphene, NiO/graphene and NiO NSs, we focused on individual NiO NSs during lithiation process. In NiO@graphene (Fig. 3a-e), the contrast of the pristine NiO NS (I) (dashed circle) is inhomogeneous (Fig. 3a). After 4 seconds (Fig. 3b), the majority (bottom-right) of the NiO NS is almost fully lithiated and has a uniform contrast (the arrows denote the expansion direction), while the residual region (top-left) remains the initial inhomogeneous contrast. We can see a smooth but distinct boundary between these two regions. Finally, the residual part finished lithiation after 6 seconds (Fig. 3c). High-resolution transmission electron microscopy (HRTEM) images and electron diffraction patterns (EDPs) show that the NiO NS changes from a polycrystalline structure to a composite of isolated Ni nanoparticles embedded in a Li_2O matrix after lithiation (Fig. S7). However, in the NiO/graphene (Fig. 3f-k), the whole NiO NS (II) (dashed circle in Fig. 3f) expands almost simultaneously (Fig. 3g-i) during lithiation. The image superimposition of the evolution process for NiO NS (I) and NiO NS (II) are shown in Figs. 3d and j, respectively, clearly indicating the different reaction kinetics between Li^+ and NiO in the two samples.

The Li^+ reaction rate with NiO highly depends on the interfacial Li^+ supply between graphene and NiO. Hence, in NiO@graphene, based on the good Li^+ diffusion provided by graphene and many interfacial Li^+ diffusion paths (blue arrows) (right in Fig. 3e), the Li^+ diffusion front on the graphene surface (red arrow) was almost the same as the reaction front of NiO. Meanwhile, the gradient distribution of Li^+ along the Li^+ diffusion direction results in the inhomogeneous lithiation of NiO in Fig. 3b. However, in NiO/graphene, due to the loose interfacial contact and few interfacial Li^+ diffusion paths (right in Fig. 3k), Li^+ transfer from graphene to NiO is much more difficult, thus hindering the Li^+ reaction with NiO. The graphene had to collect excess Li^+ to ensure the interfacial Li^+ transfer to complete the lithiation of NiO. The Li^+ will be uniformly distributed. Therefore, the lithiation of NiO in NiO/graphene is almost isotropic. The statistical data for the reaction of individual NiO NSs with Li^+ in the two samples are listed in Tables S1 and 2. From the data, we can calculate that the average reaction time for the Li^+ reacts with NiO is 5 seconds in NiO@graphene, which is 4.2 times faster than that for NiO/graphene (21 seconds), regardless of the size of NiO.

In NiO NSs, during the lithiation process, we can see the lithiation of NiO proceeding one nano-sheet after another along the Li^+ diffusion direction (See Fig. 3l-o, and Supplementary Movie S2). High-resolution transmission electron microscopy (HRTEM) images and electron diffraction patterns (EDPs) show the same transition as that in NiO@graphene (Fig. S8). When the first NiO nano-sheet (yellow) has finished its lithiation (15 seconds), the others show negligible expansion (Fig. 3m). Similarly, when the second NiO (orange) achieved full lithiation after 51 seconds, the third NiO NS remains intact (Fig. 3n). Finally, the third NiO (green) completed its lithiation after 165 seconds (Fig. 3o). As the large diffusion barrier at the NiO

surface (2.67 eV) by the first-principles calculations for Li^+ diffusion, the lithiation of the second NiO NS can start only after the first NiO particle is fully lithiated to form a continuous Li^+ conductive Li_2O matrix, as shown in Fig. 3l-o. Furthermore, as the NiO reaction proceeds, the time required to produce full lithiation of a NiO NS becomes longer and longer, indicating the greater difficulty of transporting Li^+ over a long distance. Hence, the NiO NSs exhibits the lowest Li^+ reaction rate (estimated to be 77 seconds on average). Considering the situation in the real battery fabrication, the agglomeration of NiO in NiO NSs electrode will far exceed the situation in *in-situ* TEM. A much slower Li^+ reaction kinetics will be achieved in the real battery in NiO NSs. However, in NiO/graphene (Fig. S9a) and NiO@graphene (Fig. S9b), the time required to produce full lithiation of a NiO nano-sheet is uninfluenced by the Li^+ diffusion distance, which is contrary to that in pure NiO NSs without graphene, (See Supplementary Movie S1 for NiO@graphene and Supplementary Movie S3 for NiO/graphene). The results further indicate that graphene will facilitate the homogeneous lithiation of NiO in the hybrids.

In view of the *in-situ* TEM situation, the results obtained from the TEM may correspond to the electrochemical behavior of electrode materials at a large current density in a battery. According to the electrochemical half-battery test, the capacity of NiO@graphene is 5.5 times that of NiO/graphene at a large

current density (2.5 A g^{-1}), while the NiO NS electrode became useless at the same current density (as shown in Ref. 16). These are well consistent with the *in-situ* observation, indicating graphene's significant improvement of rate capability in the hybrids.

In order to verify this, we calculated the rate capacity ratios at a large current density from the results of other studies, including Fe_3O_4 ^{38,39}, Fe_2O_3 ⁴⁰, CuO ⁴¹ (Fig. 3p). The trends of Li^+ reaction kinetics are similar to our *in-situ* (red star) observations and the corresponding electrochemical tests (pink). These results imply a common conclusion that a graphene matrix, together with an intimate interface between graphene and active materials are both essential for metal oxide electrodes to achieve a superior power density.

Meanwhile, considering the big difference between the Li^+ diffusion barrier on the NiO surface (2.67 eV) and on graphene (0.29 eV), it is strongly implied that the Li^+ behavior at large current densities in NiO@graphene should be identical in both electrochemical tests and *in-situ* TEM observations. The Li^+ diffused on the graphene and then, through the interface to react with NiO, regardless of the liquid electrolyte used in the electrochemical tests and all solid systems examined in the *in-situ* TEM observations.

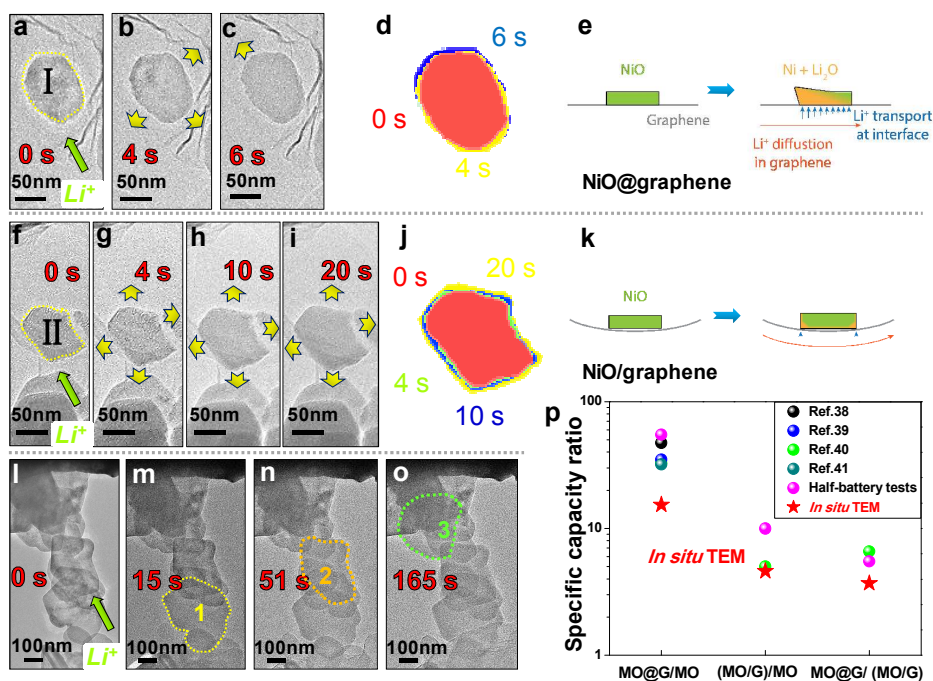


Fig. 3 Li^+ reaction kinetics with (a-e) NiO@graphene, (f-k) NiO/graphene, (l-o) NiO NSs and (p) statistical results from electrochemical tests. (a-c), (f-i) Snapshots for the Li^+ reaction with NiO in (I) NiO@graphene and (II) NiO/graphene. (d, j) Image superimposition of NiO (I) and (II) during lithiation. (e, k) Schematics of the Li^+ reaction behavior in the two samples. The blue arrows stand for the interfacial Li^+ transport paths and the length of them show the amount of Li^+ diffusion through the interface. (l-o) Snapshots for the Li^+ reaction with NiO in NiO NSs. (p) The statistical rate capacity ratio of various graphene-metal oxides at large current density discharge. The MO represents metal oxide electrodes. The MO@G/MO represents the ratio of the rate capacity of metal oxide@graphene to its corresponding metal oxide (MO) electrode. The abbreviation is similar for (MO/G)/MO and (MO@G)/(MO/G). The capacity of MO electrodes becomes almost zero at a large current density, so in order to calculate the ratio, we assumed the capacity of metal oxide electrodes at high current densities were 10 mAh/g.

Interfacial restriction of the expansion of NiO. The large volume expansion of NiO during lithiation cannot be ignored and is detrimental to the cyclic performance of batteries containing them¹⁵. From the side-view of NiO@graphene, the NiO undergoes expansions both parallel and perpendicular to the NiO NS during lithiation, but the perpendicular expansion is much greater (57%) (Fig. 4a-e). Interestingly, no noticeable parallel expansion at the interface between NiO and graphene can be observed after full lithiation. However, an obvious expansion occurs at a position away from the interface, with the largest length increase being about 10%. Meanwhile, the angle between the side edge of the NiO NS and the graphene plane changes from α (59°) to β (43°) after lithiation (Fig. 4c, d). For comparison, we studied the morphology changes during the electrochemical lithiation of NiO in NiO/graphene (Fig. 4f-j). From the side-view, the expansion of NiO occurred both parallel and perpendicular to the NiO NS. The perpendicular expansion is 48%. Meanwhile, the angle (γ) between the side edge of NiO and the graphene plane was almost unchanged after lithiation (Fig. 4h, i). Schematics for the lithiation of NiO NS in the two samples from top and side-views are shown in Figs. 4e and j.

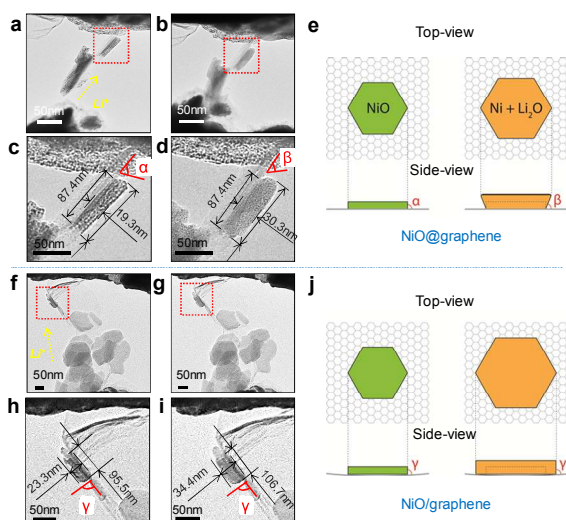
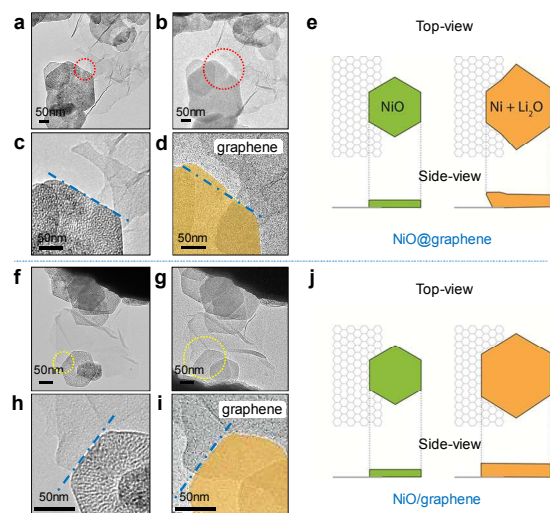


Fig. 4 Lithiation of NiO NS in (a-e) NiO@graphene and (f-j) NiO/graphene. (c, h), (d, i) Magnified views of the red dashed frames in (a, f) the pristine state and (b, g) after lithiation. (e, j) Schematics for lithiation of NiO NS in the two samples.

To confirm this interfacial restriction effect, we studied the expansion of NiO close to a graphene edge in the two samples (Fig. 5). From the top-view, the edge of a NiO NS in NiO@graphene is straight (red circle in Fig. 5a and blue line in Fig. 5c). After lithiation, expansion parallel to the NiO NS is noticeable at both sides of the graphene edge (Fig. 5b, d, and Supplementary Movie S4). The region of the NiO NS attached to the graphene has an expansion parallel to the graphene plane that is more restricted than the part that is not attached to the graphene (Fig. 5d, e). In contrast to the NiO@graphene, the expansion of



NiO NS parallel to the graphene plane is isotropic in NiO/graphene from the top-view regardless of whether the NiO NS is in contact with graphene (as shown in Fig. 5f-j).

Fig. 5 Restricting effect of graphene during lithiation. TEM images of (a, d) the pristine NiO and (b, e) NiO after lithiation in NiO@graphene and NiO/graphene, respectively. (c, f) Magnified views of dashed circles (b) (red) and (e) (blue). (g, h) Illustration of NiO expansion near graphene edges in the two samples.

These observations indicated that, in NiO@graphene, due to strong interfacial bonding, the expansion of NiO NS, parallel to the graphene plane, is highly restricted, especially at the interface (side-view). This will ensure stable connectivity between the graphene and the active materials during subsequent charge-discharge cycling, and an excellent cycling performance will be achieved in the battery. In contrast, the NiO NS in NiO/graphene debonds easily from the graphene and becomes useless during sustained expansion-shrinkage, causing capacity degradation in the battery. The statistical results of the expansion of NiO NS parallel to the graphene plane of the two samples (listed in Table S1, 2) further confirm the restrictive effect of the graphene. The electrochemical results (as shown in Ref. 16) also indicate that NiO@graphene has the largest first coulombic efficiency and the highest retention of initial capacity after 50 charge/discharge cycles, as predicted by the *in-situ* TEM observations.

We further studied the delithiation process by taking NiO/graphene as an example. After applying a reverse bias of 3.0 V, the lithiated NiO/graphene started to delithiate (Fig. S10), and the NiO NS underwent irreversible volume change after delithiation (Fig. S10a, c).⁴²

Conclusions

In summary, from the *in-situ* TEM observation, we witnessed with graphene addition, an increased Li^+ diffusion rate, improved Li^+ reaction kinetics and a facilitated homogeneous lithiation of NiO. Furthermore, in a strongly-coupled NiO@graphene, the interfacial interaction between graphene and NiO intensively enhances the Li^+ diffusion from graphene to NiO via interface for achieving a superior rate capability and strongly restricts the expansion of NiO near the interface during lithiation ensuring a stable contact between graphene and NiO during sustained expand-shrinkage of NiO for obtaining an excellent cycle stability. Supported by the electrochemical half-battery tests and first-principles calculations, this research suggests that one can optimize graphene-based lithium storage by producing strong interfacial interactions (for example, face to face connection, *in-situ* synthesis of composites). Importantly, The *in-situ* TEM results on the NiO-graphene hybrids also can be applied to other graphene-based hybrid anodes, e.g. Si, SnO_2 ⁴³⁻⁴⁵, and maybe the graphene-based hybrid cathode, e.g. $LiFePO_4$ ⁴⁶, LMO⁴⁷ (Lithium Manganese Oxide Spinel) for lithium ion batteries. Meanwhile, these findings on graphene hybrids may shed light on the improvement of other carbon hybrid systems for excellent lithium or sodium storage.

Acknowledgements

This work is supported by Ministry of Science and Technology of China (No. 2011CB932604 and 2014CB932402), National Science Foundation of China (Nos. 51221264, 51172239 and 51372253) and "Strategic Priority Research Program" of the Chinese Academy of Sciences (XDA01020304). We acknowledge helpful discussions with Dr. Dai-Ming Tang. We specially thank Mr. Bo Wu for help in EELS characterization.

Notes and references

Shenyang National Laboratory for Materials Science, Institute of Metal Research, Chinese Academy of Sciences, 72 Wenhua Road, Shenyang 110016, China. E-mail: cheng@imr.ac.cn, fli@imr.ac.cn.

Electronic Supplementary Information (ESI) is available on internet.

- Dunn, B., Kamath, H., Tarascon, J. M., Electrical energy storage for the grid: a battery of choices. *Science* **2011**, 334, 928-935.
- Bruce, P. G., Freunberger, S. A., Hardwick, L. J. & Tarascon, J.-M. Li-O₂ and Li-S batteries with high energy storage. *Nat. Mater.* **2012**, 11, 19-29.
- Bruce, P. G., Scrosati, B., Tarascon, J. M., Nanomaterials for rechargeable lithium batteries. *Angew. Chem. Int. Ed.* **2008**, 47, 2930-2946.
- Poizot, P., Laruelle, S., Grugeon, S., Dupont, L., Tarascon, J. M., Nano-sized transition-metal oxides as negative-electrode materials for lithium-ion batteries. *Nature* **2000**, 407, 496-499.
- Cabana, J., Monconduit, L., Larcher, D., Palacin, M. R., Beyond Intercalation-Based Li-Ion Batteries: The State of the Art and Challenges of Electrode Materials Reacting Through Conversion Reactions. *Adv. Mater.* **2010**, 22, E170-E192.
- Reddy, M. V., Subba Rao, G. V., Chowdari, B. V. R., Metal Oxides and Oxysalts as Anode Materials for Li Ion Batteries. *Chem. Rev.* **2013**, 113, 5364-5457.
- Lai, X.Y., Wang D., Recent advances in micro-/nano-structured hollow spheres for energy applications: From simple to complex systems. *Energy Environ. Sci.*, **2012**, 5, 5604-5618.
- Wang, J.Y., *et al.*, Accurate Control of Multishelled Co₃O₄ Hollow Microspheres as High-Performance Anode Materials in Lithium-Ion Batteries. *Angew. Chem. Int. Ed.* **2013**, 52, 6417-6420.
- Xu, S. M., α -Fe₂O₃ multi-shelled hollow microspheres for lithium ion battery anodes with superior capacity and charge retention. *Energy Environ. Sci.*, **2014**, 7, 632-637.
- Simon, P., Gogotsi, Y., Materials for electrochemical capacitors. *Nat. Mater.* **2008**, 7, 845-854.
- Zhai, Y., *et al.*, Carbon materials for chemical capacitive energy storage. *Adv. Mater.* **2011**, 23, 4828-4850.
- Dai, L., Chang, D. W., Baek, J. B., Lu, W., Carbon nanomaterials for advanced energy conversion and storage. *Small* **2012**, 8, 1130-1166.
- Liang, M., Zhi, L., Graphene-based electrode materials for rechargeable lithium batteries. *J. Mater. Chem.* **2009**, 19, 5871-5878.
- Pumera, M., Graphene-based nanomaterials for energy storage. *Energy Environ. Sci.* **2011**, 4, 668-674.
- Wu, Z.S., *et al.*, Graphene/metal oxide composite electrode materials for energy storage. *Nano Energy* **2012**, 1, 107-131.
- Zhou, G. M., *et al.*, Oxygen Bridges between NiO Nanosheets and Graphene for Improvement of Lithium Storage. *ACS Nano* **2012**, 6, 3214-3223.
- Miller, D. J., Proff, C., Wen, J. G., Abraham, D. P., Bareño, J., Observation of Microstructural Evolution in Li Battery Cathode Oxide Particles by *In-situ* Electron Microscopy. *Adv. Energy Mater.* **2013**, 3, 1098-1103.
- Becker, C. R., Strawhecker, K. E., McAllister, Q. P., Lundgren, C. A., *In-situ* Atomic Force Microscopy of Lithiation and Delithiation of Silicon Nanostructures for Lithium Ion Batteries. *ACS Nano* **2013**, 7, 9173-9182.
- Hu, Y.Y., *et al.*, Origin of additional capacities in metal oxide lithium-ion battery electrodes. *Nat. Mater.* **2013**, 12, 1130-1136.
- Ebner, M., Marone, F., Stampanoni, M., Wood, V., Visualization and Quantification of Electrochemical and Mechanical Degradation in Li Ion Batteries. *Science* **2013**, 342, 716-720.
- Liu, X., *et al.*, Distinct charge dynamics in battery electrodes revealed by *in-situ* and operando soft X-ray spectroscopy. *Nature Commun.* **2013**, 4, 2568-2578.

22. Huang, J. Y., *et al.*, *In-situ* observation of the electrochemical lithiation of a single SnO₂ nanowire electrode. *Science* **2010**, 330, 1515-1520.
23. Liu, X. H., *et al.*, *In-situ* TEM Experiments of Electrochemical Lithiation and Delithiation of Individual Nanostructures. *Adv. Energy Mater.* **2012**, 2, 722-741.
24. Su, Q. M., *et al.*, *In Situ* TEM Observation of the Electrochemical Process of Individual CeO₂/Graphene Anode for Lithium Ion Battery. *J. Phys. Chem. C.* **2013**, 117, 4292-4298
25. Su, Q. M., *et al.*, *In Situ* Transmission Electron Microscopy Observation of the Conversion Mechanism of Fe₂O₃/Graphene Anode during Lithiation-Delithiation Processes. *ACS Nano* **2013**, 7, 9115-9121.
26. Su, Q. M., *et al.*, *In Situ* Transmission Electron Microscopy Observation of Electrochemical Behavior of CoS₂ in Lithium-Ion Battery. *ACS Appl. Mater. Interfaces*, **2014**, 6, 3016-3022.
27. Islam, M. M., Bredow, T., Density Functional Theory Study for the Stability and Ionic Conductivity of Li₂O Surfaces. *J. Phys. Chem. C.* **2008**, 113, 672-676.
28. Wu, Z. S.; Ren, W. C.; Gao, L. B.; Liu, B. L.; Jiang, C. B.; Cheng, H. M. Synthesis of High-Quality Graphene with a Predetermined Number of Layers. *Carbon* **2009**, 47, 493-499.
29. Kresse, G., Furthmuller, J., Efficient iterative schemes for ab initio total-energy calculations using a plane-wave basis set. *Phys. Rev. B* **1996**, 54, 11169-11186.
30. Perdew, J. P., Burke, K., Ernzerhof, M., Generalized gradient approximation made simple. *Phys. Rev. Lett.* **1996**, 77, 3865-3868.
31. Blochl, P. E., Projector Augmented-Wave Method. *Phys. Rev. B* **1994**, 50, 17953-17979.
32. Blochl, G. Joubert, X. D., From ultrasoft pseudopotentials to the projector augmented-wave method. *Phys. Rev. B* **1999**, 59, 1758-1775.
33. Lee, S.I., *et al.*, A study of electrochemical kinetics of lithium ion in organic electrolytes. *Korean J. Chem. Eng.* **2002**, 19, 638-644.
34. Cui, Y., Zhao, X., Guo, R., Improved electrochemical performance of La_{0.7}Sr_{0.3}MnO₃ and carbon co-coated LiFePO₄ synthesized by freeze-drying process. *Electrochim. Acta* **2010**, 55, 922-926.
35. Takami, N., Satoh, A., Hara, M., Ohsaki, T., Structural and Kinetic Characterization of Lithium Intercalation into Carbon Anodes for Secondary Lithium Batteries. *J. Electrochem. Soc.* **1995**, 142, 371-379.
36. Zhou, L.J., Hou, Z. F., Wu, L. M., First-Principles Study of Lithium Adsorption and Diffusion on Graphene with Point Defects. *J. Phys. Chem. C* **2012**, 116, 21780-21787.
37. Su, D., Ford, M., Wang, G., Mesoporous NiO crystals with dominantly exposed {110} reactive facets for ultrafast lithium storage. *Sci. Rep.* **2012**, 2, 924-930.
38. Su, J., Cao, M., Ren, L., Hu, C., Fe₃O₄-Graphene Nanocomposites with Improved Lithium Storage and Magnetism Properties. *J. Phys. Chem. C* **2011**, 115, 14469-14477.
39. Zhang, M., *et al.*, Magnetite/graphene composites: microwave irradiation synthesis and enhanced cycling and rate capabilities for lithium ion batteries. *J. Mater. Chem.* **2010**, 20, 5538-5543.
40. Qu, J., *et al.*, Layer Structured α -Fe₂O₃ Nanodisk/Reduced Graphene Oxide Composites as High-Performance Anode Materials for Lithium-Ion Batteries. *Appl. Surf. Sci.* **2013**, 5, 3932-3936.
41. Wang, B., Wu, X.L., Shu, C.Y., Guo, Y.G., Wang, C.-R., Synthesis of CuO/graphene nanocomposite as a high-performance anode material for lithium-ion batteries. *J. Mater. Chem.* **2010**, 20, 10661-10664.
42. Wang, X. *et al.*, Revealing the conversion mechanism of CuO nanowires during lithiation-delithiation by *in-situ* transmission electron microscopy. *Chem. Commun.* **2012**, 48, 4812-4814.
43. Liu, H., *et al.*, Flower-like SnO₂/graphene composite for high-capacity lithium storage. *Appl. Surf. Sci.* **2012**, 258, 4917-4921.
44. Zhu, Y., *et al.*, Directing Silicon-Graphene Self-Assembly as a Core/Shell Anode for High-Performance Lithium-Ion Batteries. *Langmuir* **2012**, 29, 744-749.
45. Xue, D.J., *et al.*, Improving the Electrode Performance of Ge through Ge@C Core-Shell Nanoparticles and Graphene Networks. *J. Am. Chem. Soc.* **2012**, 134, 2512-2515.
46. Hu, L.H., Wu, F.Y., Lin, C.-T., Khlobystov, A. N., Li, L.J., Graphene-modified LiFePO₄ cathode for lithium ion battery beyond theoretical capacity. *Nature Commun.* **2013**, 4, 1687-1693.
47. Noh, H. K., Park, H.S., Jeong, H. Y., Lee, S. U., Song, H. K., Doubling the Capacity of Lithium Manganese Oxide Spinel by a Flexible Skinny Graphitic Layer. *Angew. Chem. Int. Ed.* **2014**, 126, 5159-5163.